Simulation of Local Instabilities during Crack Propagation in the Ductile-Brittle Transition Region

Geralf Hütter, Uwe Mühlich, Meinhard Kuna

Accepted Manuscript

Title: Simulation of Local Instabilities during Crack Propagation in the Ductile-Brittle Transition Region

Authors: Geralf Hütter, Uwe Mühlich, Meinhard Kuna

PII: S0997-7538(10)00151-8

DOI: 10.1016/j.euromechsol.2010.12.013

Reference: EJMSOL 2668

To appear in: *European Journal of Mechanics / A Solids*

Received Date: 20 July 2010

Revised Date: 21 December 2010

Accepted Date: 22 December 2010

Please cite this article as: Hütter, G., Mühlich, U., Kuna, M. Simulation of Local Instabilities during Crack Propagation in the Ductile-Brittle Transition Region, European Journal of Mechanics / A Solids (2011), doi: 10.1016/j.euromechsol.2010.12.013

Simulation of Local Instabilities during Crack Propagation in the Ductile-Brittle Transition Region

Geralf Hütter*, Uwe Mühlich, Meinhard Kuna

Freiberg University of Mining and Technology, Institute of Mechanics and Fluid Dynamics, Lampadiusstr. 4, 09596 Freiberg, Germany

Abstract

The crack propagation for a cohesive zone model within an elastic-plastic material under small-scale yielding conditions is simulated numerically. The resulting crack growth resistance curves show local instabilities, so-called pop-ins even for homogeneous cohesive properties if the cohesive strength lies sufficiently close to the maximum stress of the corresponding blunting solution. The formation of secondary cracks and unloading zones in front of the actual crack tip is identified as the underlying mechanism. It is found that the shape of the cohesive law has a considerable influence on the crack arrest behavior. Furthermore, requirements to the mesh resolution are derived.

Keywords: cohesive zone model, small-scale yielding, pop-in, crack arrest

1. Introduction

In fracture mechanical experiments with typical engineering metals in the ductile-brittle transition region, i.e. for low temperatures and/or dynamic loading, often sudden but limited displacement jumps are observed which are accompanied by a load drop as depicted schematically in figure 1. This

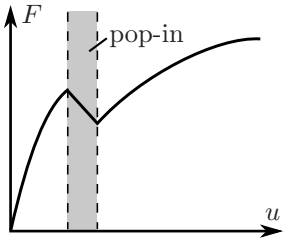

Figure 1: Load-displacement curve during pop-in

behavior is induced by a locally unstable crack propagation and termed as "pop-in" (ASTM E1290-08$^{\varepsilon 1}$, 2008). Pop-ins have been reported e.g. for steels (Ripling et al., 1982; Singh and Banerjee, 1991; Neimitz et al., 2010; Dzioba et al., 2010), armco iron (Srinivas et al., 1989), welded joints (Sumpter, 1991a,b), aluminum alloys (Firrao et al., 1993) or ductile cast iron (Kobayashi and Yamada, 1994).

In many cases, these local instabilities are ascribed to the initiation and arrest of cracks propagating with a cleavage mechanism. In general, the loads at which pop-ins occur scatter considerably for several samples of the same material. That is why mostly the initiation of these local instabilities is attributed to microstructural inhomogeneities such as inclusions or segregations of embrittling chemical components. The inhomogeneities are sometimes termed as "local brittle zones".

Firrao et al. (1993) and Neimitz, Galkiewicz, and Dzioba (Neimitz et al., 2010; Dzioba et al., 2010) reported the formation of secondary cracks in front of the main crack tip in the context of pop-ins. A corresponding micrograph is depicted in figure 2. Neimitz, Galkiewicz, and Dzioba as well as Sumpter (1991b) draw a close interrelationship between pop-ins and plastic deformations at the crack tip.

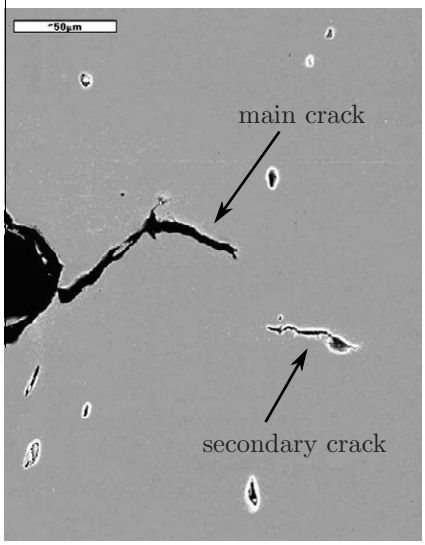

Figure 2: Secondary crack in the cross-section of a specimen of a ferritic-bainitic steel from an experiment interrupted shortly before the presumed pop-in (Neimitz et al., 2010)

The assumption of local brittle zones as reason for pop-ins

*Corresponding author
Email addresses: Geralf.Huetter@imfd.tu-freiberg.de (Geralf Hütter), Uwe.Muehlich@imfd.tu-freiberg.de (Uwe Mühlich), Meinhard.Kuna@imfd.tu-freiberg.de (Meinhard Kuna)

motivated the modeling by means of locally fluctuating material properties. For instance, the works of Tvergaard, Needleman and co-workers (Tvergaard and Needleman, 1993; Gao et al., 1996; Needleman and Tvergaard, 2000) or Kabir et al. (2007) can be cited out of this group.

The latter research group applied a cohesive zone model with locally fluctuating strength within an elastic-plastic bulk material. However, they also obtained pop-ins for their first computations with *homogeneous* cohesive properties. Likewise, Lin et al. (1999) as well as Li and Siegmund (2004) observed local instabilities with cohesive zone models of homogeneous strength within elastic-plastic material. The reasons of the occurrence of pop-ins was not investigated further.

Siegmund and Needleman (1997) simulated the crack propagation in a CCT-specimen under impact loading also by means of a homogeneous cohesive zone model within viscoplastic material. For increased plastic contributions they observed crack arrest accompanied by the formation of secondary loading zones around the crack tip. The formation of secondary cracks has been observed for cohesive zone models within constraint metal layers by Lin et al. (1997). The decrease of the loading capacity due to a priori existent secondary cracks has been extensively studied in the literature, e.g. by Tomokazu and Yasufumi (1977), Smith (1988) and Siegmund and Brocks (2000).

The objective of the present study is to further investigate the pop-in behavior predicted by a cohesive zone in plastic bulk material and to gain deeper insight into the underlying mechanism. To exclude possible effects of the geometry and viscosity the limit case of small-scale yielding is simulated and the bulk material is modeled as rate independent. Requirements to the mesh resolution are derived. A special focus is drawn on the influence of the shape of the cohesive law.

2. Problem Formulation

2.1. Boundary-Value Problem

Following the approach of Tvergaard and Hutchinson (1992, 1994, 1996), the crack propagation under mode I is investigated by means of a cohesive zone under plane strain small-scale yielding conditions. As pop-ins are highly dynamic processes inertia is taken into account. The bulk material is described by an isotropic hypoelastic-plastic formulation for large strains with J_2-yield surface and isotropic hardening. A one-parametric power law of hardening is utilized, so that it provides an uniaxial response between true stress and logarithmic strain of

$$\varepsilon = \begin{cases} \sigma/E & \sigma < \sigma_\mathrm{Y} \\ \sigma_\mathrm{Y}/E\,(\sigma/\sigma_\mathrm{Y})^{1/N} & \text{else} \end{cases} . \tag{1}$$

A bi-linear cohesive law as depicted in figure 3 is used, whereby the traction t refers to the actual configuration. The work of separation Γ_0 is related to the critical crack opening displacement δ_c and the cohesive strength $\hat{\sigma}$ via

$$\Gamma_0 = \int_0^{\delta_\mathrm{c}} t\,\mathrm{d}\delta = \frac{1}{2}\hat{\sigma}\delta_\mathrm{c} . \tag{2}$$

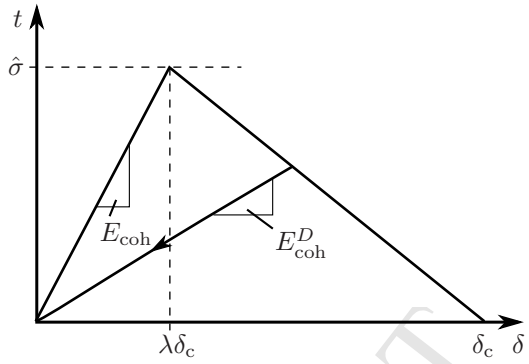

Figure 3: Bi-linear traction-separation law

The dimensionless shape parameter $\lambda \in [0, 1]$ describes the initiation of softening with respect to the critical separation δ_c. The bi-linear relation has the advantage that despite its simplicity the effects of the influence of the shape of the cohesive law on the predicted crack growth resistance can be investigated by varying the only dimensionless shape parameter λ. If not specified otherwise the shape parameter is set to $\lambda = 0.24$ which lies in the region of typical cohesive laws.

The unloading branch in the softening region in figure 3 expresses the irreversible character of the material separation process and is quantified by a damage variable

$$D = 1 - \frac{E^D_{\mathrm{coh}}}{E_{\mathrm{coh}}} \tag{3}$$

as ratio between slope E^D_{coh} of the cohesive law and its initial value E_{coh}.

Following the publications of Tvergaard and Hutchinson (1992, 1994, 1996) reference values for the normalization are defined as

$$K_0 = \sqrt{E'\Gamma_0}\,, \qquad R_0 = \frac{1}{3\pi}\left(\frac{K_0}{\sigma_\mathrm{Y}}\right)^2 . \tag{4}$$

Thereby the term $E' = E/(1-\nu^2)$ abbreviates Young's modulus under plane strain conditions. The value K_0 is the fracture toughness of the cohesive model within a purely elastic material and the length R_0 scales with the size of the plastic zone. The intrinsic length contained within the initial slope E_{coh} of cohesive law is described by

$$R_{\mathrm{init}} = \frac{E'}{2E_{\mathrm{coh}}} . \tag{5}$$

The factor two is incorporated for convenience as the results in section 4 show.

Although dynamic simulations are performed the loading has to be applied quasi-statically ensuring that the crack propagation and arrest during pop-in are not influenced by changes of the magnitude of loading. Consequently, the time elastic waves need to pass characteristic distances of the problem has to be small compared to the time scale of loading $\tau_\mathrm{L} = K_I^{\max}/\dot{K}_I$.

This applies especially to the slower shear waves which propagate with speed c_s requiring

$$\frac{R_0}{c_s} \ll \tau_L \,. \tag{6}$$

2.2. Measure of Crack Extension

In classical fracture mechanics, the crack tip is assumed as ideally sharp, so that the crack length is defined uniquely. However, this is not the case for the employed cohesive zone model where the softening region has a finite extension.

In the present study the crack tip is defined as center of the softening zone, whereby the damage variable D is chosen as weight as depicted schematically in figure 4a. Thus, the increase of the crack length is computed as

$$\Delta a = \int_0^\infty D \, \mathrm{d}x \,. \tag{7}$$

Thereby, without loss of generality it is assumed that the crack propagates along the positive x-direction starting at $x = 0$. If a secondary crack occurs, the smeared definition (7) incorporates the extension of the secondary crack as sketched in figure 4b. In any case, the results obtained with different possible definitions of crack growth differ considerably only in the stadium of crack initiations. Besides, definition (7) has the advantage to be defined as well for cohesive laws approaching the traction-free state only asymptotically.

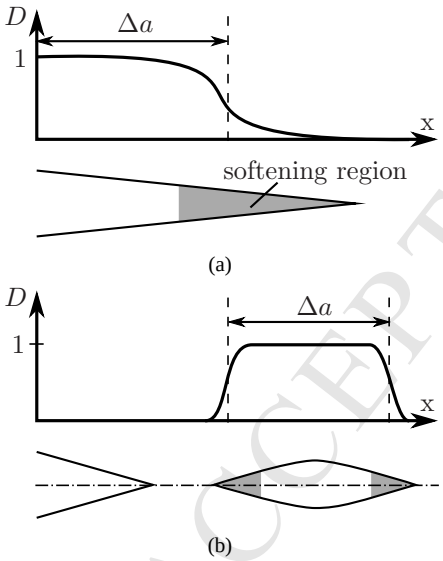

Figure 4: Smeared measure of crack extension for (a) softening at the primary crack tip and (b) growth of a secondary crack

3. Numerical Implementation

3.1. FE-Model

The described boundary value problem is solved with the commercial FE-code Abaqus. A boundary layer of radius A_0 is spatially discretized with a mesh as shown in figure 5. The radius is chosen with $A_0 = 30\,(K_I^{\max}/K_0)^2 R_0$ whereby $K_I^{\max}$ denotes the maximum loading. In order to avoid volumetric locking in the plastic zone and for performance reasons quadrilateral elements with bilinear shape functions and reduced integration[1] are used. Due to the symmetry, only one half of the problem needs to be discretized. A region of width $B_0 = 6.5\,R_0$ is fine-meshed with equilateral elements of edge length Δ. Section 4 is dedicated to the determination of the necessary mesh resolution.

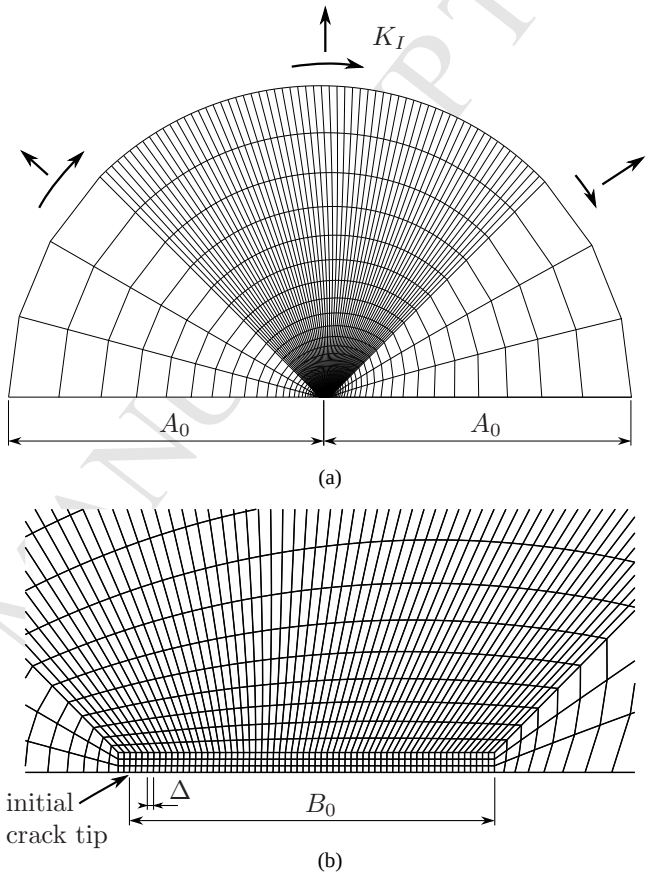

Figure 5: Finite element mesh of (a) whole model and (b) near the crack tip

The cohesive elements available in Abaqus implement constitutive laws defined in terms of nominal tractions. However, for the present study a true stress formulation is desired. The employed implementation is outlined in Appendix A.

In section 2.1 it was pointed out that quasi-static conditions are present if the time stress waves need to pass characteristic distances of the problem is short compared to the characteristic time scale of loading. For the introduced FE-model of finite extent this applies to the outer radius A_0 of the model thus imposing the stronger requirement $A_0/c_s \ll \tau_L$.

[1] The default value of the software of an hourglass stiffness of 0.5% of the largest eigenvalue of the element stiffness is employed. For a sample computation fully integrated, hybrid elements were employed instead. The differences were negligible.

The following computations are performed with implicit time integration. In the initial stadium the crack propagates stably so that as initial condition the nodal velocities are set to zero. The mass density is specified so that values of $R_0/c_s = 1/30,000\,\tau_L$ are obtained. This choice guarantees sufficiently small inertia forces during stable crack propagation but does not lead to too small time increments in the instable region. So the computations require several hundred to a few thousand time increments each.

3.2. Fracture Mechanical Evaluation

During the dynamic process of pop-in the loading of the process zone, expressed by the dynamic stress intensity factor K_{Id}, differs from the applied loading K_I. A dimensional analysis for the linear-elastic far-field shows, that the interrelationship between both values can only have the structure

$$K_{Id} = k\,(\Delta\dot{a}/c, \nu)\; K_I\,. \tag{8}$$

Thereby it was taken into account, that for the quasi-static loading under consideration the problem cannot depend on time explicitly. The connecting factor $k\,(\Delta\dot{a}/c, \nu)$ is termed the *universal function of crack tip speed*. The strictly monotonic function $k\,(\Delta\dot{a})$ equals unity for $\Delta\dot{a} = 0$ and vanishes at RAYLEIGH speed $\Delta\dot{a} = c_R$. During crack propagation the crack tip loading K_{Id} corresponds to the crack growth resistance:

$$K_R = K_{Id}\,. \tag{9}$$

As the crack growth $\Delta a(t)$ has to be determined anyway and the loading K_I is known, equation (8) allows to extract the current resistance K_R comfortably. The smeared crack length definition (7) leads to smooth $\Delta a(t)$ curves that can be reliably differentiated numerically. In oder to shorten the complicated analytical expression, Freund (1989) proposed the approximation

$$k\,(\Delta\dot{a}) \approx \frac{1 - \Delta\dot{a}/c_R}{\sqrt{1 - \Delta\dot{a}/c_s}} \tag{10}$$

which is used in the following.

4. Necessary Mesh Resolution

First of all, the admissible element size for an accurate solution of the boundary value problem declared in section 2.1 has to be determined. Especially the point of damage initiation within the cohesive zone, i.e. when the maximum stress $\sigma_{\varphi\varphi}^{\max}$ normal to the crack plane in the ligament reaches the cohesive strength $\hat{\sigma}$ for the first time, needs to be resolved. For these considerations the softening behavior of the traction-separation law does not need to be taken into account. This can be accomplished by choosing a cohesive strength larger than the maximum ligament stress $\sigma_{bl}^{\max}$ of the corresponding blunting solution. The latter has been investigated extensively (e.g. Rice, 1968; Rice and Johnson, 1970; McMeeking, 1977) yielding maximum stresses of $\sigma_{bl}^{\max} = 3\ldots5\,\sigma_Y$ depending on the hardening properties. As no instable crack propagation occurs without softening inertia need not be taken into account for this investigation.

Under these circumstances the only intrinsic length is contained within the initial slope of the cohesive law as defined in equation (5). Dimensional considerations allow to specify the functional interrelationship

$$\frac{\sigma_{\varphi\varphi}^{\max}}{\sigma_Y} = f\left(\frac{K_I}{\sigma_Y\sqrt{R_{init}}}, \frac{E}{\sigma_Y}, N, \nu\right) \tag{11}$$

for the maximum ligament stress $\sigma_{\varphi\varphi}^{\max}$.

The two limit cases for small respectively large dimensionless loading $K_I/\left(\sigma_Y\sqrt{R_{init}}\right)$ can be identified. For small stress intensity factors the bulk material remains elastic. As the whole problem is linear then the maximum stress is proportional to K_I and occurs at the crack tip. Under these conditions the energy release rate of the elastic far-field equals the cohesive work at the crack tip leading to the maximum ligament stress of

$$\sigma_{\varphi\varphi}^{\max} = \frac{K_I}{\sqrt{R_{init}}}\,. \tag{12}$$

For large loadings $K_I/\left(\sigma_Y\sqrt{R_{init}}\right) \to \infty$ the intrinsic length becomes negligibly small compared to the size of the plastic zone so that the sketched problem approaches the blunting solution asymptotically. Thus, in the intermediate range between these two limit cases for increasing loading the location of maximum stress moves from the crack tip towards a position in front of the tip.

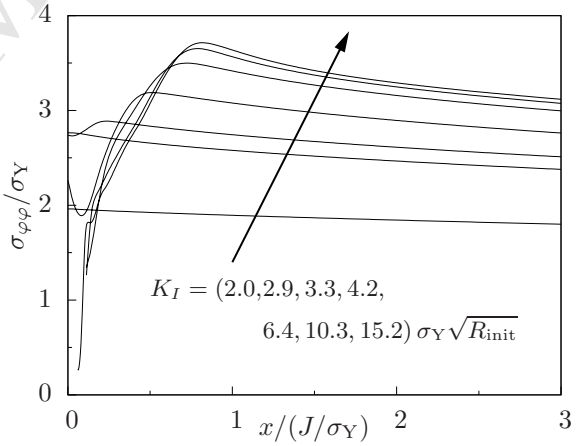

Figure 6: Transition from the elastic to the blunting solution: normal stresses $\sigma_{\varphi\varphi}$ in the ligament for a linear cohesive law ($N = 0.1$, $\nu = 0.3$, $\Delta = 0.125\,\sigma_Y/E\,R_{init}$)

The evolution of the stresses in the ligament with the loading for the linear cohesive law has been investigated numerically by means of the described finite element model. Within the fine meshed region around the crack tip an element size of $\Delta = 0.125\,\sigma_Y/E\,R_{init}$ is used. The normal stresses $\sigma_{\varphi\varphi}$ in the ligament are plotted in figure 6 for a set of parameters and show the transition from the linear to the blunting solution.

The increase of the maximum stress $\sigma_{\varphi\varphi}^{\max}$ in the ligament with the loading in the dimensionless form (11) is depicted

in figure 7. The diagram also incorporates the linear solution (12) and the corresponding blunting solution $\sigma_{\mathrm{bl}}^{\max}$ as asymptote. The loading point when the maximum stress $\sigma_{\varphi\varphi}^{\max}$ departs from the crack tip to a local maximum in front of it for the first time is marked by $\times$.

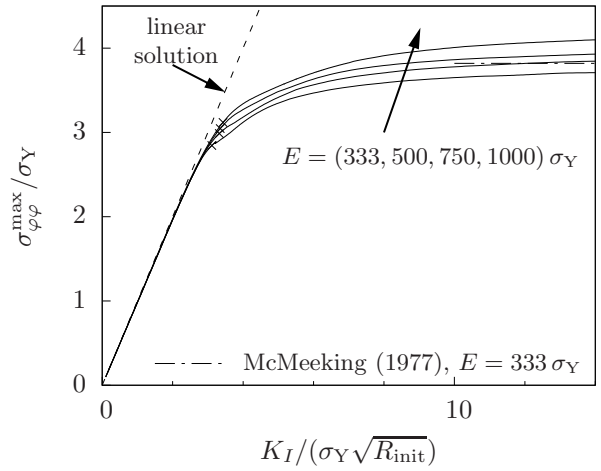

Figure 7: Maximum stress $\sigma_{\varphi\varphi}^{\max}$ in the ligament for a linear cohesive law as function of dimensionless loading (marked by $\times$: $\sigma_{\varphi\varphi}^{\max}$ as local maximum in front of crack tip for the first time; $N = 0.1$, $\nu = 0.3$, $\Delta = 0.125\,\sigma_{\mathrm{Y}}/E\,R_{\mathrm{init}}$)

As figure 7 shows the stress $\sigma_{\varphi\varphi}^{\max}$ has a value of about $\sigma_{\varphi\varphi}^{\max} \approx 70\% \ldots 80\%\,\sigma_{\mathrm{bl}}^{\max}$ when the maximum occurs in front of the crack tip for the first time. In this range the solution hardly differs from the linear one (12). In the dimensionless form the corresponding load K_I is only slightly higher and thus amounts to about $K_I/\left(\sigma_{\mathrm{Y}}\sqrt{R_{\mathrm{init}}}\right) \approx \sigma_{\mathrm{bl}}^{\max}/\sigma_{\mathrm{Y}}$. The position $x_{\max}$ of the maximum stress scales with J/σ_{Y}. Hence, in the transition region the mesh needs to be fine enough to resolve local fields changing within a distance of $J/\sigma_{\mathrm{Y}} = K_I^2/(E'\sigma_{\mathrm{Y}})$ so that the element size has to be chosen with

$$\Delta \ll \left(\frac{\sigma_{\mathrm{bl}}^{\max}}{\sigma_{\mathrm{Y}}}\right)^2 \frac{\sigma_{\mathrm{Y}}}{E'} R_{\mathrm{init}}\,. \tag{13}$$

For the bi-linear cohesive law this can be rearranged to

$$\Delta \ll 0.5\,\frac{\hat{\sigma}}{\sigma_{\mathrm{Y}}}\lambda\delta_{\mathrm{c}}\,. \tag{14}$$

Thereby, it was taken into account that the maximum stress $\sigma_{\varphi\varphi}^{\max}$ equals the cohesive strength $\hat{\sigma}$ at the transition point. Consequently, in the transition region the elements need to be considerably smaller than the critical cohesive opening δ_{c}. However, as figure 7 shows the loads to reach higher ligament stresses after the transition rapidly increase and so does the position of the maximum stress. Thus, for higher cohesive strengths the requirements to the mesh resolution are less strict. This applies also to the linear and nearly linear range below the transition point where the stresses around the crack tip vary over distances scaling with R_{init} only.

Since the whole parameter range including the transition region is to be investigated, an element size $\Delta = 0.2\,\delta_{\mathrm{c}}$ is used for the following computations which turned out to be an appropriate choice.

5. Results

5.1. Crack Growth Resistance Curves

A typical computed crack growth resistance curve is depicted in figure 8. It shows an oscillatory behavior, i.e. after the dynamic propagation the crack arrests and further loading is necessary in order to drive the crack again. The coarse mesh with $\Delta = 10\,\delta_{\mathrm{c}}$ does not resolve the local instabilities and the steep initial tearing, thus confirming the considerations in section 4.

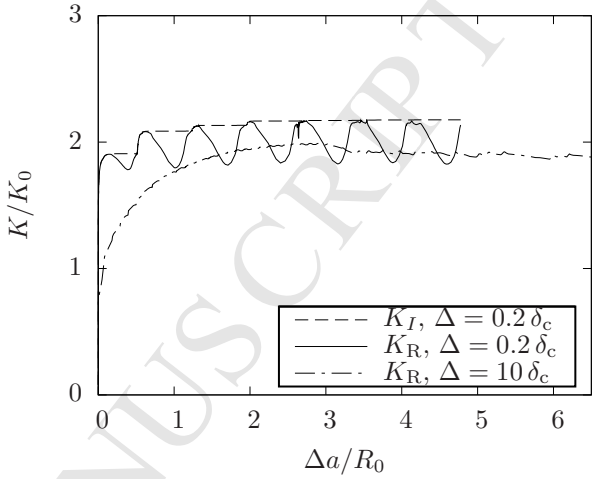

Figure 8: Snap-through in crack growth resistance curve ($\hat{\sigma}/\sigma_{\mathrm{Y}} = 3.6$, $E/\sigma_{\mathrm{Y}} = 333$, $N = 0.1$, $\nu = 0.3$, $\lambda = 0.24$)

In principle, it would be possible that the crack arrest is induced by waves reflected at the artificially introduced boundary at radius A_0. The crack tip velocity $\Delta\dot{a}$ during instable crack propagation is plotted in figure 9 and indicates a crack arrest after about $0.0004\,\tau_{\mathrm{L}}$. This span is short compared to the time $A_0/c \approx 0.0025\,\tau_{\mathrm{L}}$ the faster longitudinal elastic waves of speed c need to reach the boundary. Consequently, the crack arrest is inherent to the problem. The reflections only cause the small disturbance during the forth crack arrest in the curve for the fine mesh in figure 8.

The evolution of the damage variable D in the ligament as depicted in figure 10 shows, that the pop-in occurs when the first point becomes completely damaged. However, this point does *not lie at* the crack tip but *in front* of it. When in this region the cohesive zone completely has lost its stress-carrying capacity it forms a secondary crack. The latter shields the plastic zone of the main crack tip leading to elastic unloading within this region. The missing contribution of this zone to the plastic dissipation results in decreasing crack growth resistance. Subsequently, the secondary crack tip begins to blunt inducing the same behavior in front of its own tip. The work required for the plastic deformation of the formed crack tip is responsible for the anew increasing crack growth resistance. This mechanism repeats. The residual plastic strains in the wake behind the

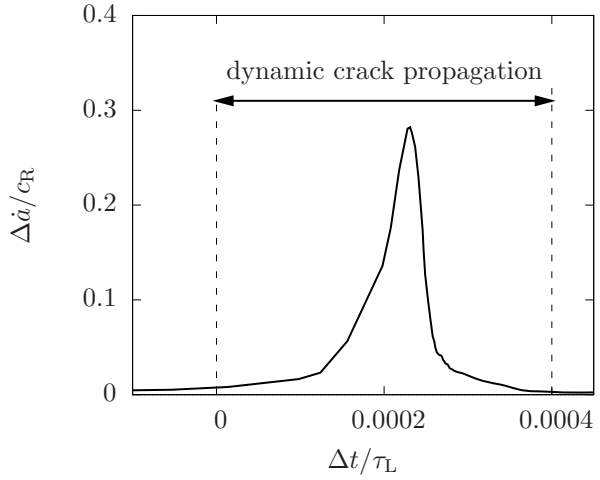

Figure 9: Crack tip velocity during first instable propagation ($E/\sigma_Y = 333$, $N = 0.1$, $\nu = 0.3$, $\hat{\sigma}/\sigma_Y = 3.6$, $\lambda = 0.24$, $\Delta = 0.2\,\delta_c$)

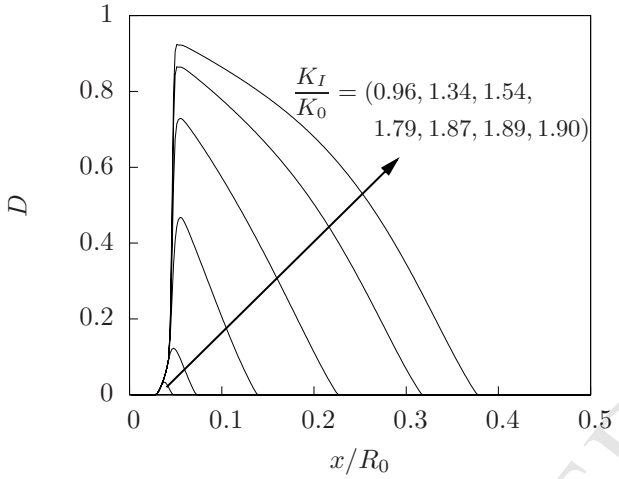

Figure 10: Damage evolution in the ligament before the first pop-in ($\hat{\sigma}/\sigma_Y = 3.6$, $E/\sigma_Y = 333$, $N = 0.1$, $\nu = 0.3$, $\lambda = 0.24$, $\Delta = 0.2\,\delta_c$)

current crack tip as depicted in figure 11 attest to the periodic behavior.

However, after the formation of the secondary crack the next local instability occurred already before a further crack was induced. Apparently, partly softening in front of the secondary crack tip and unloading of the surrounding material is sufficient for a locally decreasing crack growth resistance. Nevertheless, the plastically deformed ligament between primary and secondary crack, the so-called stretch zone, persists until several periods of the mechanism have been passed.

In the following the influence of several parameters is investigated.

5.2. Influence of the Shape of the Cohesive Law

First of all, the shape parameter λ is varied. The crack growth resistance curves obtained for different values are depicted in figure 12 and show a strong dependence. So the periodicity

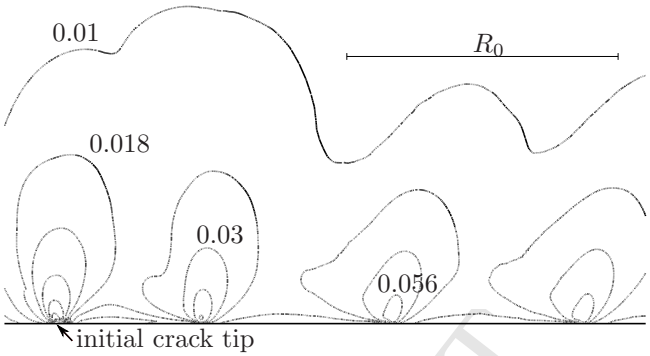

Figure 11: Equivalent plastic strain in the wake behind the current crack tip (depicted with respect to the reference configuration; $E/\sigma_Y = 333$, $N = 0.1$, $\nu = 0.3$, $\hat{\sigma}/\sigma_Y = 3.6$, $\lambda = 0.24$, $\Delta = 0.2\,\delta_c$)

Δa_{instab} of the instability as well as its amplitude decrease with increasing λ. Additionally, larger values of λ cause a delayed damage initiation, i.e. a higher value at the intersection with the ordinate axis in figure 12. This has the consequence that for high values of the shape parameter the first pop-in occurs already at the load level of the steady-state toughness K_R^{ss}. Referring to Tvergaard and Hutchinson (2008) the latter is defined as maximum value of the crack growth resistance curve. In contrast, for low values of λ the load can be further increased after the first crack arrest.

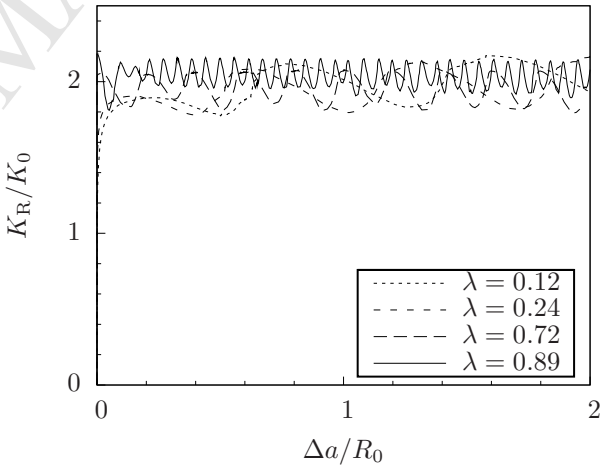

Figure 12: Crack growth resistance curves for different values of the cohesive shape parameter λ ($\hat{\sigma}/\sigma_Y = 3.6$, $E/\sigma_Y = 333$, $N = 0.1$, $\nu = 0.3$, $\Delta = 0.2\,\delta_c$)

Figure 13a shows that the steady-state toughness K_R^{ss} is only moderately influenced by the shape parameter. Conversely, the effect of λ on Δa_{instab} is almost independent of the cohesive strength $\hat{\sigma}$ as figure 13b indicates. In addition, the period Δa_{instab} tends to zero if the value of λ is increased towards unity.

The reason for the dependency of the period Δa_{instab} on the shape parameter λ is that a higher value of λ means that the softening region of the traction-separation relation becomes steeper in favor of a smaller initial slope. But the faster the cohesive

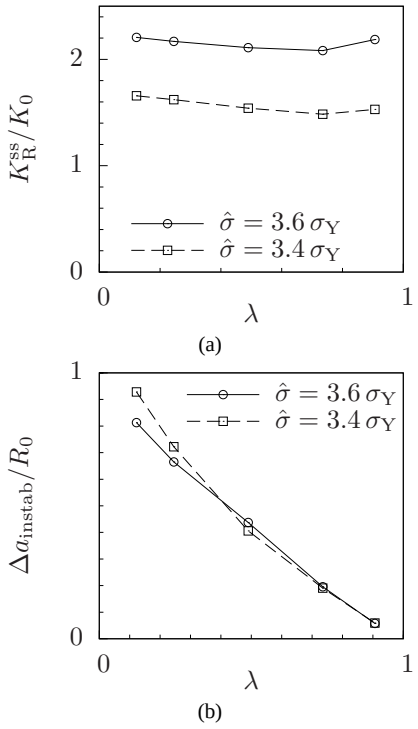

Figure 13: (a) Steady-state fracture toughness K_R^{ss} and (b) periodicity Δa_{instab} as function of the shape parameter λ ($E/\sigma_Y = 333$, $N = 0.1$, $\nu = 0.3$, $\Delta = 0.2\,\delta_c$)

zone softens the faster the damaging region in front of the crack tip forms a secondary crack and unloading zones that shield its predecessor.

5.3. Influence of the Cohesive Strength

In the following the cohesive strength $\hat{\sigma}$ is varied relative to the initial yield stress σ_Y. The resulting crack growth resistance curves are depicted in figure 14. As expected, the steady-state fracture toughness K_R^{ss} increases with higher ratios $\hat{\sigma}/\sigma_Y$. The figure shows, that intermediate instabilities can be observed as soon as the plastic contribution to the crack growth resistance exceeds about 20 to 30 %.

6. Discussion

The present study dealt with the simulation of mode I crack growth using a bi-linear cohesive zone model under small-scale yielding conditions. It was found that for several parameter sets local instabilities occur, the so-called pop-ins. The results indicate that softening in front of the crack tip is responsible for pop-ins. For a cohesive law with linear initial region the binary information whether damage initiates at or in front of the crack tip depends on the cohesive strength and the properties of the bulk material only but for dimensional reasons not on the value of the initial slope (see section 4). Thus, it stands to reason, that under small scale yielding a pop-in mechanism is predicted by all cohesive zone models with linear initial range and an immediately following softening, if the cohesive strength lies

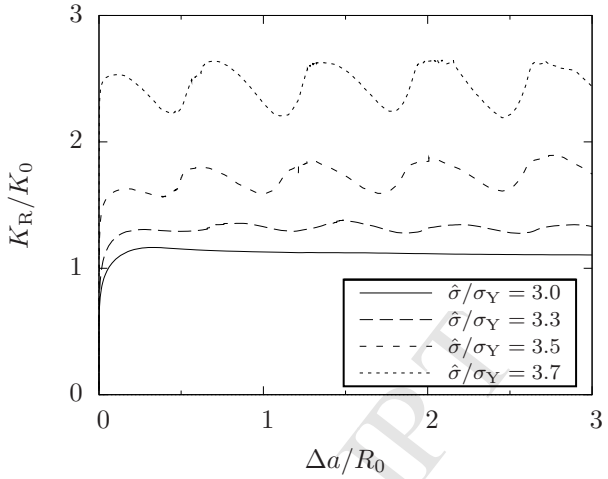

Figure 14: Equilibrium crack growth resistance curves for different cohesive strengths ($E/\sigma_Y = 333$, $N = 0.1$, $\nu = 0.3$, $\Delta = 0.2\,\delta_c$)

sufficiently close to the maximum stress of the corresponding blunting solution.

It was found that the necessary element size in order to resolve the damage initiation scales with the width of the linear initial region of the cohesive law. Presumably, the same restriction applies to the softening range which controls the formation of secondary cracks.

Parameter studies have shown, that in contrast to the fracture toughness the crack jump width during pop-in and the possible further loading capacity is considerably influenced by the shape parameter of the cohesive law. Hence, the latter should be fitted to experiments addressing these material properties.

The fact that all numerical simulations have been performed with homogeneous material properties implies that local brittle zones are not inevitably necessary for pop-ins. Rather, this phenomenon is determined by the mean material properties as well. However, in the simulations the pop-ins appeared only in that range where the steady-state toughness strongly depends on the cohesive strength. This is in accordance with the experimental observations that already small fluctuations of the local strength lead to significant scatter of the loads at which pop-ins occur.

In the following the results of the present study are compared to those reported in the literature. Simulations of crack propagation with a cohesive zone model under small-scale yielding have been performed by a number of authors (Tvergaard and Hutchinson, 1992, 2008; Tvergaard, 2010; Lin and Cornec, 1996; Lin, 1996; Wei and Hutchinson, 1997; Niordson, 2001). For static simulations using a tri-linear cohesive law with wide plateau, Tvergaard and Hutchinson (Tvergaard and Hutchinson, 1992, 2008; Tvergaard, 2010) observed an instable point, i.e. a local maximum in the R-curves, for some parameter sets. However, behind this point they found an asymptotically decreasing crack growth resistance without further local maxima. In the present study the limit case of quasi-static loading is considered so that an influence of the mass density on the computed R-curves is excluded. Hence, the results should be comparable

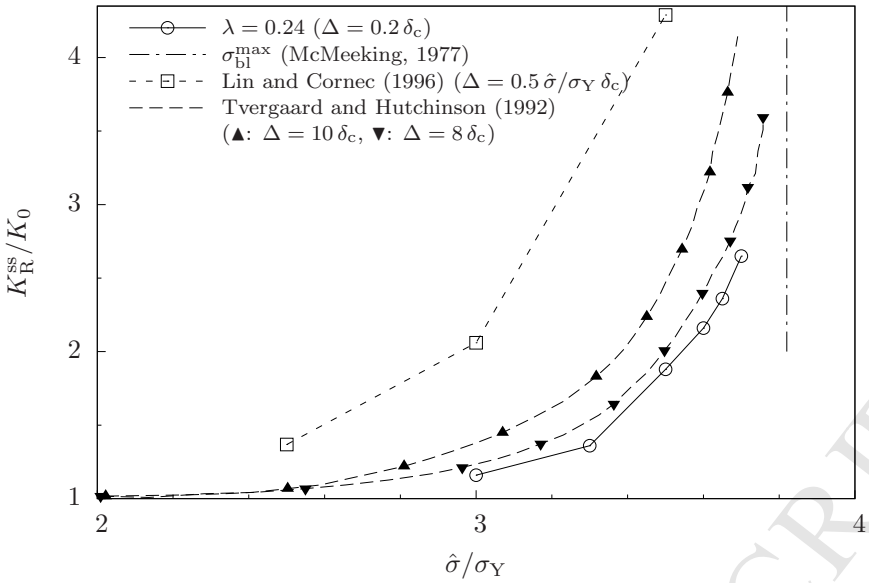

Figure 15: Steady-state toughness K_R^{ss} in comparison with data from literature ($E/\sigma_Y = 333$, $N = 0.1$, $\nu = 0.3$)

to those of Tvergaard and Hutchinson in principle. Possibly, the cohesive law employed by these authors leads to less pronounced instabilities. For their investigations Tvergaard and Hutchinson used an element size of $\Delta = 10\,\delta_c$ within the process zone. Figure 8 shows, that with this mesh resolution the present model exhibits a similar asymptotic behavior. Lin and Cornec (Lin and Cornec, 1996; Lin, 1996) simulated the crack growth only "until the applied K ... almost ceases to increase".

Wei and Hutchinson (1997) as well as Niordson (2001) investigated the same problem but employed an Eulerian-type approach to compute the steady-state fracture toughness directly. However, by excluding the non-stationary terms a priori they would not have been able to resolve possible instabilities.

Performing dynamic simulations under large-scale yielding with a cohesive law of exponential type Siegmund and Needleman (1997) substantiated a crack arrest independent of wave reflections. As in the present study these authors observed locally instable crack propagation already for moderate plastic contributions to the crack growth resistance.

In figure 15 the computed steady-state fracture toughness values are plotted in comparison with data from literature. In addition to the curve for the cohesive law with a wide plateau (marked by ▲ in the figure), Tvergaard and Hutchinson (1992) published the steady-state toughnesses obtained with a cohesive law with narrower plateau and a slightly refined mesh (marked by ▼ in the figure). Especially the latter is in good accordance with the results of the present study. Only the data of Lin and Cornec (1996) differ considerably. Figure 15 indicates a trend towards higher toughness values for more compact cohesive laws, i.e. those with a wider plateau. All curves exhibit the asymptotic behavior discussed by Tvergaard and Hutchinson that the toughness becomes arbitrarily large if the cohesive strength $\hat{\sigma}$ approaches the maximum ligament stress σ_{bl}^{max} of the associated blunting solution resulting in a high sensitivity within this region.

If the employed model is used to describe the ductile-brittle transition of an engineering metal the cohesive zone represents the cleavage mechanism. In this context the term ductile is covered by the model in the sense of a relevant plastic contribution of the matrix material to the crack growth resistance. For the experiments of Neimitz, Galkiewicz, and Dzioba cited in the introduction in the corresponding temperature region the values of the lower shelf toughness and yield stress are $K_0 = 25 \ldots 35\,\mathrm{MPa\,m^{0.5}}$ and $\sigma_Y = 300 \ldots 400\,\mathrm{MPa}$ (Dzioba et al., 2010) so that the reference length amounts to $R_0 = 0.4 \ldots 1.4\,\mathrm{mm}$. In the simulations the extension of the stretch zone at formation of a secondary crack lies in the range of several to some ten percent of R_0 depending on the value of the shape parameter. This is in accordance with the micrograph depicted in figure 2.

Acknowledgments

The financial support of this investigation by the Deutsche Forschungsgemeinschaft (German Science Foundation) under contract KU 929/14-1 is gratefully acknowledged. The authors thank the student Mr. A. Burgold for his great commitment in generating the finite element meshes for the present study.

References

Abaqus, 2009. Abaqus Theory Manual v6.9. ABAQUS, Inc. and Dassault Systèmes.

ASTM E1290-08$^{\varepsilon 1}$, 2008. Standard Test Method for Crack-Tip Opening Displacement (CTOD) Fracture Toughness Measurement.

Dzioba, I., Gajewski, M., Neimitz, A., 2010. Studies of fracture processes in Cr-Mo-V ferritic steel with various types of microstructures. Int. J. Pres. Ves. Pip. 87 (10), 575–586.

Firrao, D., Doglione, R., Ilia, E., 1993. Thickness constraint loss by delamination and pop-in behavior. In: Hackett, E. M., Schwalbe, K., Dodds, R. (Eds.), Constraint Effects on Fracture. No. 1171 in ASTM STP. pp. 289–305.

Freund, L. B., 1989. Dynamic Fracture Mechanics. Cambridge University Press.

Gao, X., Shih, C., Tvergaard, V., Needleman, A., 1996. Constraint effects on the ductile-brittle transition in small scale yielding. J. Mech. Phys. Solids. 44 (8), 1255–1282.

Kabir, R., Cornec, A., Brocks, W., 2007. Simulation of quasi-brittle fracture of lamellar γTiAl using the cohesive model and a stochastic approach. Comp. Mater. Sci. 39 (1), 75–84.

Kobayashi, T., Yamada, S., 1994. Evaluation of static and dynamic fracture toughness in ductile cast iron. Metall. Mater. Trans. A. 25 (11), 2427 – 2437.

Li, W., Siegmund, T., 2004. An analysis of the indentation test to determine the interface toughness in a weakly bonded thin film coating - substrate system. Acta. Mater. 52 (10), 2989–2999.

Lin, G., 1996. Numerical investigation of crack growth behavior using a cohesive zone model. Dissertation, TU Hamburg-Haburg.

Lin, G., Cornec, A., 1996. Characteristics of crack resistance: Simulation with a new cohesive model. Mat.-wiss. u. Werkstofftech. 27 (5), 252–258, in German; results in part also published by **?**.

Lin, G., Kim, Y.-J., Cornec, A., Schwalbe, K. H., 1997. Fracture toughness of a constrained metal layer. Comp. Mater. Sci. 9 (1–2), 36–47.

Lin, G., Meng, X.-G., Cornec, A., Schwalbe, K.-H., 1999. The effect of strength mis-match on mechanical performance of weld joints. Int. J. Fracture. 96 (1), 37–54.

McMeeking, R. M., 1977. Finite deformation analysis of crack-tip opening in elastic-plastic materials and implications for fracture. J. Mech. Phys. Solids. 25 (5), 357–381.

Needleman, A., Tvergaard, V., 2000. Numerical modeling of the ductile-brittle transition. Int. J. Fracture. 101 (1), 73–97.

Neimitz, A., Galkiewicz, J., Dzioba, I., 2010. The ductile-to-cleavage transition in ferritic Cr-Mo-V steel: A detailed microscopic and numerical analysis. Eng. Fract. Mech. 77 (13), 2504–2526.

Niordson, C. F., 2001. Analysis of steady-state ductile crack growth along a laser weld. Int. J. Fracture. 111 (1), 53–69.

Rice, J. R., 1968. A path independent integral and the approximate analysis of strain concentration by notches and cracks. J. Appl. Mech. 35 (2), 379–386.

Rice, J. R., Johnson, M. A., 1970. The role of large crack tip geometry changes in plane strain fracture. In: Kanninen, M. F. (Ed.), Inelastic Behavior of Solids. McGraw-Hill, New York, pp. 641–672.

Ripling, E., Mulherin, J., Crosley, P., 1982. Crack arrest toughness of two high strength steels (AISI 4140 and AISI 4340). Metall. Mater. Trans. A. 13 (4), 657–664.

Siegmund, T., Brocks, W., 2000. Modeling crack growth in thin sheet aluminum alloys. In: Halford, G. R., Gallagher, J. P. (Eds.), Fatigue and Fracture Mechanics: 31st Volume. No. 1389 in ASTM STP. pp. 475–485.

Siegmund, T., Needleman, A., 1997. A numerical study of dynamic crack growth in elastic-viscoplastic solids. Int. J. Solids. Struct. 34 (7), 769–787.

Singh, U., Banerjee, S., 1991. On the origin of pop-in crack extension. Acta. Metall. Mater. 39 (6), 1073–1084.

Smith, L. K., 1988. Macrocrack-multiple defect interaction considering elastic, plastic and viscoplastic effects. Masterthesis, Faculty of the School of Engineering, Air Force Institute of Technology.

Srinivas, M., Malakondaiah, G., Rama Rao, P., 1989. On 'apparent pop-in' during ductile fracture toughness testing being related to the yield-point phenomenon in armco iron. Scripta. Metall. Mater. 23 (9), 1627–1632.

Sumpter, J. D. G., 1991a. Pop-in and crack arrest in an HY80 weld. Fatigue. Fract. Eng. M. 14 (5), 565–578.

Sumpter, J. D. G., 1991b. Pop-in fracture: observations on load drop, displacement increase, and crack advance. Int. J. Fracture. 49 (3), 203–218.

Tomokazu, M., Yasufumi, I., 1977. Pop-in behavior induced by interaction of cracks. Eng. Fract. Mech. 9 (1), 17–24.

Tvergaard, V., 2010. Effect of pure mode I, II or III loading or mode mixity on crack growth in a homogeneous solid. Int. J. Solids. Struct. 47 (11-12), 1611–1617.

Tvergaard, V., Hutchinson, J. W., 1992. The relation between crack growth resistance and fracture process parameters in elastic-plastic solids. J. Mech. Phys. Solids. 40 (6), 1377–1397.

Tvergaard, V., Hutchinson, J. W., 1994. Effect of T-stress on mode I crack growth resistance in a ductile solid. Int. J. Solids. Struct. 31 (6), 823–833.

Tvergaard, V., Hutchinson, J. W., 1996. Effect of strain-dependent cohesive zone model on predictions of crack growth resistance. Int. J. Solids. Struct. 33 (20-22), 3297–3308.

Tvergaard, V., Hutchinson, J. W., 2008. Mode III effects on interface delamination. J. Mech. Phys. Solids. 56 (1), 215–229.

Tvergaard, V., Needleman, A., 1993. An analysis of the brittle-ductile transition in dynamic crack growth. Int. J. Fracture. 59 (1), 53–67.

Wei, Y., Hutchinson, J. W., 1997. Steady-state crack growth and work of fracture for solids characterized by strain gradient plasticity. J. Mech. Phys. Solids. 45 (8), 1253–1273.

Appendix A. Cohesive Elements

The cohesive zone is implemented by linear elements which include a priori the symmetry condition as depicted in figure A.16. The according shape functions are

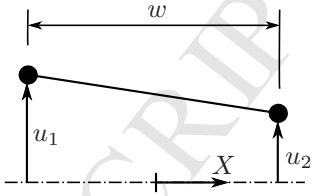

Figure A.16: Linear cohesive element for symmetric separation

$$N_1(x_0) = \frac{1}{2}(1+\eta)\,, \quad N_2(x_0) = \frac{1}{2}(1-\eta)\,, \quad \eta = \frac{2x_0}{w_0}\,. \tag{A.1}$$

Here and in the following the subscript $(\,)_0$ refers to the value of a property with respect to the reference configuration. For a single integration point the contribution of a single element to the nodal forces of both nodes is equal and takes the value

$$P_1^y = P_2^y = \frac{1}{2}wt \quad \text{with} \quad t = t\,(2u_\mathrm{m}, D)\,. \tag{A.2}$$

The traction t depends on twice the mid-point displacement $u_\mathrm{m} = 1/2\,(u_1 + u_2)$ from the symmetry line and internal variables as the damage D in the present case,

Such cohesive elements can be implemented by modifying a standard element so that it contributes the same nodal forces (A.2) under all possible load histories. For this task, four-noded quadrilaterals with reduced integration as shown in figure A.17 come into operation. First of all, symmetric element deformations, i.e. $u_x^i = u_x^{i+2}$ and $u_y^i = -u_y^{i+2}$ for $i = 1, 2$, are enforced in order to ensure that the integration points remain at the symmetry plane. Under these constraints, the shape functions of the two remaining nodes $i = 1, 2$ for the x- respective y-displacements are

$$N_i^x(x_0, y_0) = N_i(x_0) \quad \text{and} \quad N_i^y(x_0, y_0) = \frac{2y_0}{h_0} N_i(x_0)\,. \tag{A.3}$$

The corresponding contributions to the nodal forces have the value

$$P_i^x = whd\left[\sigma_{xx}\frac{\partial N_i^x}{\partial x} + \sigma_{xy}\frac{\partial N_i^y}{\partial y}\right]_\mathrm{IP} = dh\sigma_{xx} \tag{A.4}$$

$$P_i^y = whd\left[\sigma_{xy}\frac{\partial N_i^y}{\partial x} + \sigma_{yy}\frac{\partial N_i^y}{\partial y}\right]_\mathrm{IP} = dw\sigma_{yy} \tag{A.5}$$

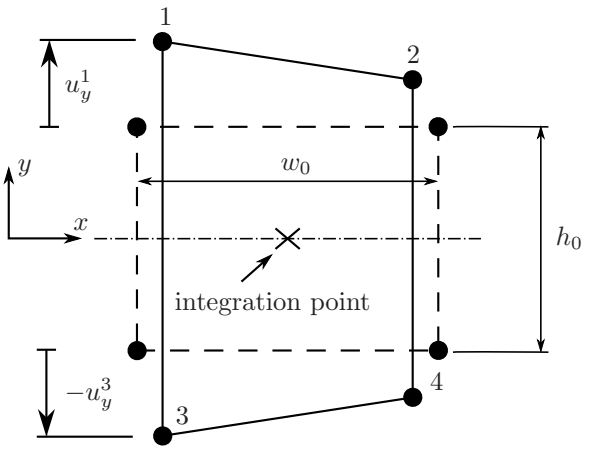

Figure A.17: Four-noded quadrilateral with reduced integration under symmetric deformation

The brackets have to be evaluated at the integration point so that the terms connected to shear stresses vanish. Furthermore, d denotes the out-of-plane thickness of the element and $h = h_0 + u_\mathrm{m}$ the intermediate height in the actual configuration.

Comparing equations (A.2) and (A.5) shows that if the thickness of the plane element is chosen with $d = 1/2$ (with respect to unit thickness of the remaining model), the stress σ_{yy} can be identified as the cohesive traction t. The horizontal nodal forces P_i^x need to vanish.

In order to obtain the desired traction-separation law, the Hashin-constitutive law, an orthotropic effective stress-type damage model originally intended for fiber-reinforced composites (Abaqus, 2009) is utilized. The material axes are aligned with the direction of cohesive separation and the Poisson-numbers are set to zero. Under the applied constraints the principal axes of loading cannot rotate, so that the hypoelastic formulation can be integrated to

$$t = (1 - D) E_y^{\mathrm{elem}} \log\left(1 + \frac{u_\mathrm{m}}{h_0}\right). \tag{A.6}$$

Here and in the following the superscript $(\ )^{\mathrm{elem}}$ denotes equivalent properties of the cohesive elements (which have no physical meaning). A comparison of (A.6) with the desired traction-separation law implies two measures. Firstly, the element height needs to be chosen with $h_0 \gg \delta_\mathrm{c}$ such that $\log(1 + u_\mathrm{m}/h_0) \approx u_\mathrm{m}/h_0$. Secondly, this allows to identify the Young's modulus in direction of separation E_y^{elem} of the cohesive element as $E_y^{\mathrm{elem}}/h_0 = E_{\mathrm{coh}}$. In the computations, values $h_0/\delta_\mathrm{c} = 50$ are used. In addition, it has to be ensured that the horizontal nodal forces (A.4) vanish. A Young's modulus E_x^{elem} equal to zero would be no problem in principal but is excluded by the input preprocessor of Abaqus. For all computations, a value of $E_x^{\mathrm{elem}} h = 10^{-9}\, E R_0$ is used. Possible couplings due to out-of-plane constraints are avoided by using plane stress elements.

The last aspect is concerned with the damage evolution law. The utilized Hashin-damage model originally is intended for a spatially continuous description. Abaqus regularizes the solution by introducing mesh dependent softening. For this purpose the program calculates a characteristic length L^{elem} from the element dimensions. In the case of the considered rectangular elements with width w_0 and height h_0 and reduced integration, this quantity takes the value $L^{\mathrm{elem}} = \sqrt{h_0 w_0}$. Abaqus calculates the dissipated work of failure under the stress-strain curve as $\Gamma_\varepsilon = \Gamma^{\mathrm{elem}}/L^{\mathrm{elem}}$, which is connected to the desired work of separation by the factor element height h_0. So the material property to be handed over to the program is $\Gamma^{\mathrm{elem}} = \sqrt{w_0/h_0}\,\Gamma_0$.